Jäsberg, Ari; Puisto, Antti; Leppänen, Ilona; Koponen, Antti I.; Alava, Mikko J.

Online detection of orientation of cellulose nanocrystals in a capillary flow with polarization-sensitive optical coherence tomography

Published in:
Cellulose

DOI:
10.1007/s10570-023-05072-4

Published: 01/04/2023

Document Version
Publisher's PDF, also known as Version of record

Cellulose (2023) 30:3539–3550
https://doi.org/10.1007/s10570-023-05072-4

ORIGINAL RESEARCH

Online detection of orientation of cellulose nanocrystals in a capillary flow with polarization-sensitive optical coherence tomography

Ari Jäsberg · Antti Puisto · Ilona Leppänen · Antti I. Koponen · Mikko J. Alava

Received: 4 May 2022 / Accepted: 19 January 2023 / Published online: 2 March 2023

Abstract Significant importance in the stiffness of materials, such as filaments and films, made of elongated components, has been attributed to orientation. Thus, the control of orientation during the manufacturing of materials has been the target of process optimization for long time. Measuring orientation during the process allows to better grasp the means to control it. In fact, such online tools would enable on-fly process control and optimization improving the flexibility with regards to the raw materials used, and the application requirements. In this article, we will discuss a method based on polarization-sensitive optical coherence tomography utilized as a light-weight online measurement tool of particle (here cellulose nanocrystals) orientation for the purposes of manufacturing next generation products by providing the appropriate interpretation of the retardation images with the help of modelling.

Keywords Cellulose nanocrystals · Optical coherence tomography · Orientation · On-linedetection · Modeling

Supplementary Information The online version contains supplementary material available at https://doi.org/10.1007/s10570-023-05072-4.

A. Jäsberg · A. I. Koponen
VTT Technical Research Centre of Finland Ltd, Koivurannantie 1, 40400 Jyvaskyla, Finland
e-mail: ari.jasberg@vtt.fi

A. I. Koponen
e-mail: Antti.Koponen@vtt.fi

A. Puisto (✉) · M. J. Alava
Department of Applied Physics, Aalto University, P.O. Box 11100, FI-00076 Aalto, Espoo, Finland
e-mail: antti.puisto@vtt.fi

M. J. Alava
e-mail: Mikko.Alava@aalto.fi

I. Leppänen
VTT Technical Research Centre of Finland Ltd, Tietotie 4E, 02150 Espoo, Finland
e-mail: ilona.leppanen@vtt.fi

Introduction

Cellulose nanocrystals (CNCs) are an emerging biodegradable material that attracts strong interest due to its high mechanical strength, possibility to modify its chemical or physical conditions, and its optical properties (George and Sabapathi 2015; Habibi et al. 2010). CNCs are typically manufactured from cellulose using strong acid hydrolysis. The surface chemistry and the size of CNC particles is dictated by the hydrolysis conditions and cellulose source. CNC particles are strongly elongated the aspect ratio being typically between 10 and 100. Due to their strength and high aspect ratio, CNC particles can be used as a reinforcement in many materials. Promising results have been obtained e.g. with filaments and fibers (Chen et al. 2014; Shrestha et al. 2018), films (Tatsumi et al. 2015; Kim et al. 2021),

and three-dimensional printing (Hausmann et al. 2018). Here controlled assembly of CNC particles is highly important for optimizing the strength properties of the produced materials (Reising et al. 2012).

CNC particles have shown great promise in improving the mechanical properties of many materials. However, their potential can be fully realized only if the orientation of the CNC particles can be optimized. Like other rod-like particles (Gunes et al. 2008; Pujari et al. 2011; Leahy et al. 2017), CNC particles tend to align in the direction of flow under shear when the time scale of the shear rate is low enough to overcome the characteristic relaxation time of rotational (Brownian) diffusion of their suspensions (Alizadehgiashi et al. 2018; Tsvetkov et al. 2017). The orientation of CNC particles in the final product can thus be improved by utilizing shear-induced alignment (Rosén et al. 2020). Other possibilities include flow focusing (Gowda et al. 2019) and extensional flow field (Pignon et al. 2003). Thus, understanding the alignment of CNC particles under various flow conditions is an important problem for materials science.

Typically the orientation may be determined from the final structure. Here various means from optical microscopy imaging to different scattering methods or even scanning electron microscopy and atomic force microscopy may be used. However, the process to form a sample, which allows these types of experiments is manifold: the dispersion is pumped, transferred via piping, laid, and solidified. Therefore, improvements to alignment in such a complex process occur typically as a result of trial and error involving adjusting the sub-processes according to intuition. online measurement of the orientation would greatly speed up the development of these processes.

Online monitoring of the alignment of particles at different parts of the process is often times cumbersome for an industrial-type setting. Small angle X-ray scattering (SAXS)(Rosén et al. 2020, 2018) and small angle neutron scattering (SANS) (Sawada et al. 2021) are viable and accurate tools for the purpose in a scientific environment. They, however, rely on heavy and expensive machinery that is not as feasible to be used to monitor an industrial process. On the other hand, the rheo-optical studies are often time- and labor-intensive and require complicated experimental setups (Fuller 1990).

Above critical mass fraction, CNC particles form liquid crystalline phases in aqueous CNC suspensions (Shafiei-Sabet et al. 2012). Self-organization usually begins when CNC mass fraction exceeds 5–6% (Parker et al. 2018). These suspensions affect the polarization state of light and are strongly birefringent materials. Birefringence is also observed with lower mass fractions when the CNC particles are ordered e.g. by shear-induced orientation.

Polarization of light has been widely utilized in the analysis of the orientation of CNC particles both in capillaries (Alizadehgiashi et al. 2018; Rosén et al. 2020), and in rotational rheometers (Shafiei-Sabet et al. 2012; Kádár et al. 2021). A novel option for polarization-based orientation analysis is polarization-sensitive optical coherence tomography (PS-OCT) (Hee et al. 1992) (de Boer et al. 2017). It has the advantage over other polarization-based applications that it gives local information of the polarization state while other methods give only an integrated polarization effect across the flow geometry.

Orientation of rod-like particles in a particle suspension connects to the suspension rheology: when particles are aligned with the flow field, they resist the flow less compared to their cross-directional counterparts. In practice under shear flow non-interacting particles experience a rotation (Jeffery orbits) (Ingber and Mondy 1994). During the rotation, the angular velocity of the particle decreases when it is aligned, and reaches its maximum when it is perpendicular to the shear. This creates a time average orientation for the individual particles. The duration of the full Jeffery orbit may be estimated by $T = 2\pi r_e/\dot{\gamma}$ (Mason and Manley 1956), where r_e is roughly 0.7 times the aspect ratio. For the CNC particles studied here this is roughly $136/\dot{\gamma}$. At higher mass fractions, repulsively interacting stiff particles tend to form phases familiar from liquid crystals. Attractively interacting particles may even form aggregates, flocs, or superstructures, which may again align with the flow field (Blaser 2000; Adachi et al. 2019).

Rheologically suspensions consisting of anisotropic particles exhibit shear thinning and time dependence at any significant particle concentrations (Sepehr et al. 2004). In a process, this couples to the stress distribution imposed by the process conditions. In extreme cases this may lead to shear localization effects and shear banding. However, for instance in capillary flows this kind of rheological behavior leads

to diminishing shear rates at the center of the capillary leading to poor alignment at these regions. The width of this regime depends on the shear thinning exponent of the fluid. At large shear thinning exponents this may lead to a situation where significant portion of the particles is very poorly oriented due to the lack of shear.

In this work, we report the results of experimental studies, based on PS-OCT, and simulations of flow-induced alignment of rod-like cellulose nanocrystals in a laminar, fully developed, capillary flow. We will analyze the results both in the context of a simple optical model and an orientation model based on Fokker–Planck equation. We have organized the manuscript in the following way: First, we will introduce the reader to the materials and methods applied, then we will discuss our results, and finish the manuscript in our concluding remarks.

Materials and methods

In this section we will introduce the materials and methods used.

Polarization-sensitive optical coherence tomography

Optical coherence tomography (OCT) is a well-established technique for structural imaging of semi-transparent materials at the micrometer scale (Swanson et al. 1991; Chen et al. 1997). OCT has been traditionally used for medical and biological applications, but its use is increasing in other fields of science and technology (Drexler and Fujimoto 2008; Koponen and Haavisto 2020). OCT utilizes low-coherence, near-infrared light to measure the reflectivity of the sample as a function of depth. By acquiring several side-by-side depth profiles (A-scans), a 2D or 3D tomographic image can be obtained for the structure of the sample. OCT can be used for the structural analysis of turbid and opaque materials. The achievable OCT imaging depth is typically in the range of a few millimeters, but it depends strongly on the studied material.

Doppler optical coherence tomography (DOCT) is an extension of OCT. It can be used for measuring the velocity field (in the direction of the measurement beam) inside the studied sample simultaneously with structural imaging. Due to high OCT temporal resolution (typically tens of kHz) DOCT enables acquiring sharp images of e.g. fast flowing suspensions.

Polarization-sensitive OCT (PS-OCT) adds measurement of the polarization state of the back-scattered light to the OCT technique (Hee et al. 1992; de Boer et al. 2017). PS-OCT thus enables the measurements of local polarization properties which depend on the micro-structure of the material. The polarization state of light can be changed e.g. by birefringent materials that have a refractive index that depends on the polarization and propagation direction of light. Birefringent material causes a relative delay between two orthogonal polarization states of light which is known as phase retardation. PS-OCT can be used for measuring the local retardation in the material. Other quantities obtained with the PS-OCT are the local optic axis (the direction along which a ray of transmitted light suffers no birefringence) and local degree of polarization. The latter quantity is useful for materials that depolarize the incident polarized light, resulting in an arbitrary polarization state of the light.

The PS-OCT device used in this study was TEL 220 PSC2–Spectral Domain PS-OCT System from Thorlabs. The central wavelength of the device is 1300 nm, axial resolution in the direction of the light beam is 3.7 µm in water, and the lateral resolution of the used optical lens is 13 µm. In this study, the rate of one-dimensional A-scans was 5.5 kHz, thus one cross-sectional image consisting of 250 A-scans was acquired in 45 ms.

Cellulose nanocrystals

The Celluforce nanocrystals were obtained as a powder. The CNC powder was dispersed in water by adding 5 wt% of powder through a sieve, while mixing it simultaneously with a magnetic stirrer. Once all CNC powder was added, the dispersion was mixed for 1 h. Subsequently, the dispersion was ultra-sonicated with the ultrasound energy of 250 J/mL under an ice bath to remove any remaining aggregates.

The ultrasonicated suspensions are stable for reasonably long times, but they will start forming aggregates given enough time. Due to this, and owing to the fact that the crystals themselves are inert towards the ultrasonication, the CNC solutions were ultrasonicated for a 2 min time before the usage.

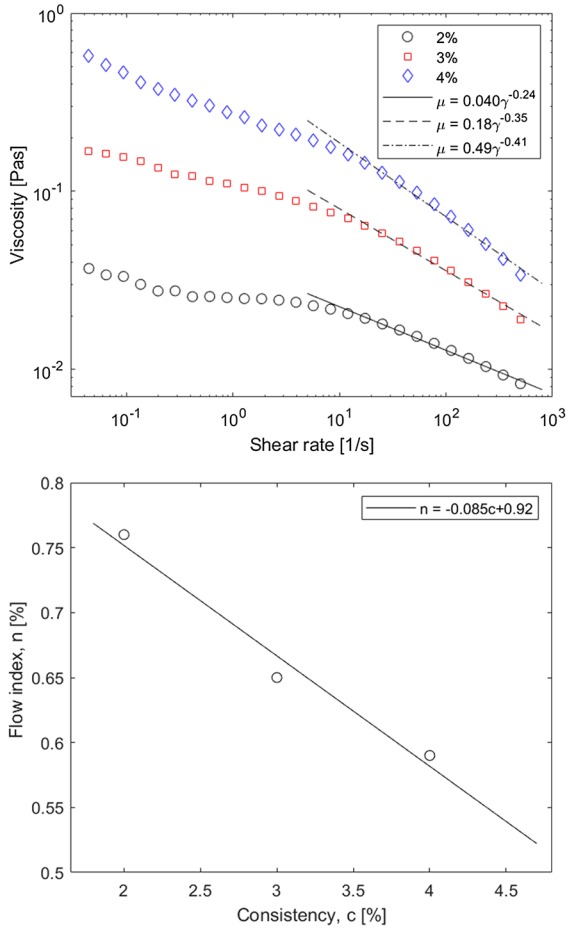

Fig. 1 Rheological characteristics of the CNC suspensions under scrutiny. Upper panel: flow curves as measured using a rotational rheometer, lower panel: flow behavior index n based on a power law $\mu = K\dot{\gamma}^{n-1}$ fit to the rheological data at shear rates $\dot{\gamma} > 10$

Rheological characterization

The rheological characterization of the suspensions was performed using a rotational rheometer (Anton Paar MCR302) employing a cone-and-plate setup (CP50-1, cone angle 0.984°) with a diameter of 49.96 mm and a 0.099 mm gap. The sample was loaded in the setup with a pipette. The steady-state shear viscosity data was gathered using an increasing shear rate ramp consisting of 26 discrete shear rates from 0.05 to 500 1/s. The timeout for each point was 120 s. The obtained viscosity-shear rate curves are shown in Fig. 1. For all mass fractions the slope of the viscosity - shear rate curves increased with higher shear rates. Such behavior has been observed also by others and our results are qualitatively similar to those e.g. by Shafiei-Sabet et al. (2012).

Retardation

Here we make a simple attempt to rationalize the retardation images obtained from PS-OCT experiments. In the context of PS-OCT, the retardation change in a small element of thickness ds is proportional to the variation of the index of refraction Δn. The retardation change may be expressed as

$$d\Gamma = \frac{2\pi \cdot ds \cdot \Delta n}{\lambda_0}, \tag{1}$$

where λ_0 is the wavelength of the light in a vacuum (Wiesauer et al. 2006; de Boer and Milner 2002). Additionally, as the OCT probe uses a telecentric lens, the light rays leave the probe in a parallel fashion. Therefore, simulating the retardation images reduces to simple ray tracing in a material with a locally defined index of refraction. In the case of elongated particles, such variation in the index of refraction is determined by the orientation distribution.

Power-law model

A simple attempt to describe the local Δn may be approached by analyzing the rheograms of Fig. 1. There a power-law dependence of the stress as a function of shear rate may be observed with high shear rates. Thus, we may consider the rheology of the material to follow a power-law constitutive model

$$\tau = K\dot{\gamma}^k. \tag{2}$$

When we additionally assume laminar flow, the local shear stress follows from Stokes' solution for the Hagen-Poisseuille flow, which reads

$$\tau(r) = \frac{r}{2}\frac{\Delta p}{\Delta L}, \tag{3}$$

where $\frac{\Delta p}{\Delta L}$ is the pressure gradient in the pipe and r is the radial distance from the center of the capillary. Demanding Eq. (2) to hold at all radial coordinates in

Eq. (3) allows solving for the local shear rate, which becomes

$$\dot{\gamma}(r) = Ar^{\frac{1}{k}}, \tag{4}$$

where A is a constant dependent on the flow rate. Notice that Eq. (4) holds only in the high-shear-rate regime.

Next, we advance a step by further hypothesising that the birefringence of the material has a power-law dependence on the local shear rate, that is, the variation of the index of refraction follows

$$\Delta n(r) = C_n \dot{\gamma}(r)^m. \tag{5}$$

here C_n and m are constants dependent on the CNC concentration. These constants encapsulate the rotational diffusivity and the particle orientation susceptibility to shear. Now this completes the model and allows to compute the retardation images using ray tracing. Naturally this model has the limitation that Δn diverges at infinite shear rate, while in reality this function must be bounded at both ends.

Orientation model

By fitting the power-law model to the experimentally obtained retardation plots we can recover a function for the radial dependence of the index of refraction Δn. Then we can attempt to match this function using a more evolved orientation model. For the purpose, we implemented a Fokker-Planck equation based orientation model in a capillary flow scenario. Such models are still under heavy development, and there remain limitations in their capabilities to predict the correct rheological behavior of such suspensions having different fiber-fiber interactions (Butler and Snook 2018). The model applied here is based on a previous work by Ma et al. (2008) and since we are not further developing the model, for the purposes of the present manuscript we review only its essential parts. The model evolves an orientation distribution having the time development

$$\frac{\partial \Psi(\boldsymbol{\rho})}{\partial t} = \frac{\partial}{\partial \boldsymbol{\rho}}\left(D_r \frac{\partial \Psi(\boldsymbol{\rho})}{\partial \boldsymbol{\rho}}\right) - \frac{\partial}{\partial \boldsymbol{\rho}}\left(\Psi(\boldsymbol{\rho})\frac{\partial \boldsymbol{\rho}}{\partial t}\right), \tag{6}$$

where t is the time, Ψ is the orientation distribution, $\boldsymbol{\rho}$ is the unit vector aligned in the particle axis direction, D_r is the rotary diffusion, and $\frac{\partial \boldsymbol{\rho}}{\partial t}$ is modelled using Jeffery's equation at large aspect ratios

$$\frac{\partial \boldsymbol{\rho}}{\partial t} = \nabla \boldsymbol{v} \cdot \boldsymbol{\rho} - (\boldsymbol{\rho}^{\intercal} \cdot \mathbf{D} \cdot \boldsymbol{\rho})\boldsymbol{\rho}, \tag{7}$$

where $\mathbf{D}$ is the rate of deformation tensor. At this point it is worth mentioning, that the model assumes relatively weak interactions between the particles. The parameter D_r encapsulates the effects of inter-fiber interactions and Brownian diffusion on the rotation. In this work it is treated as a fitting parameter adjusted based on the rheological data. A more fundamental discussion on rotational diffusion in fiber suspensions is summarized by Petrie (1999). The orientation distribution is first initialized to a homogeneous one, where all the angles have equal probability, and then evolved directly using the backwards differentiation formulas (BDF) method of the SUNDIALS library (Hindmarsh et al. 2005) avoiding the closure approximation required by the alternative tensorial solution.

From the particle orientation distribution Ψ, we compute the second and fourth-order orientation tensors $\mathbf{A}_2$ and $\mathbf{A}_4$, which, as suggested by Advani and Tucker III (1987), relate to many material properties, such as viscosity, thermal conductivity, and elasticity by the means of orientation averaging. The components of the orientation tensors are computed (following the notation by Advani and Tucker III (1987))

$$A_{ij} = \oint \rho_i \rho_j \Psi(\boldsymbol{\rho}) d\boldsymbol{\rho} \tag{8}$$

and

$$A_{ijkl} = \oint \rho_i \rho_j \rho_k \rho_l \Psi(\boldsymbol{\rho}) d\boldsymbol{\rho}, \tag{9}$$

for $\mathbf{A}_2$ and $\mathbf{A}_4$, respectively, where the integral goes over all $\boldsymbol{\rho}$. These will be later on referred to as $\langle \boldsymbol{\rho}\boldsymbol{\rho} \rangle$, and $\langle \boldsymbol{\rho}\boldsymbol{\rho}\boldsymbol{\rho}\boldsymbol{\rho} \rangle$

Specifically, the $\mathbf{A}_4$ connects the orientation distribution to rheology by a constitutive law (Ma et al. 2008; Dinh and Armstrong 1984)

$$\boldsymbol{\sigma} = -P\mathbf{I} + 2\eta \mathbf{D} + \boldsymbol{\tau} \tag{10}$$

$$\boldsymbol{\tau} = 2\eta N_p (\mathbf{A}_4 : \mathbf{D}). \tag{11}$$

here P is the pressure, η the fluid viscosity, $\boldsymbol{\tau}$ the orientation stress, which includes one more independent fitting parameter N_p which relates to the solids concentration, particle aspect ratio, and temperature, among others. Such a model is not exactly perfect, neglecting many effects such as inter-fiber interactions, yet it is assumed to capture the qualitative behavior of such systems.

We incorporate the capillary flow geometry by coupling the orientation model to the appropriate Stokes equation for the pipe flow, for which the axial momentum reads

$$\frac{dp}{dz} = \frac{1}{r}\frac{\partial(r\sigma_{zr})}{\partial r}, \tag{12}$$

where r is the radial coordinate and $\frac{dp}{dz}$ is the pressure drop along the axial direction. Now replacing σ_{zr} with that computed using Eq. (10) and discretizing the capillary along the radial coordinate allows for a numerical solution of the evolution of the capillary flow front in time. The volumetric flow rate is then controlled by iteratively adjusting the pressure drop. This assumes the flow profile to be unique at steady state - i.e. the time-evolution of the flow front does not significantly alter the shape of the velocity profile.

Orientation is typically characterized in materials by an orientation order parameter $S_2 = (3\langle\cos^2\theta\rangle - 1)/2$ (Frka-Petesic et al. 2015). Here, $\langle\rangle$ denotes the average over the orientation distribution function of the crystals. The order parameter is zero for an isotropic distribution, $S_2 = +1$ corresponds to full orientation of the crystals along the main direction $\theta = 0$ (capillary axis in this study), and $S_2 = -1/2$ corresponds to perpendicular orientation of the crystals with respect to the main direction. In the simulations the orientation distribution is known, and this allows one to quantify the particle orientation directly using the Hermans' orientation parameter (HOP) by computing $\mathrm{HOP} = 3\langle\boldsymbol{\rho}\boldsymbol{\rho}\rangle_{ii}/2 - \frac{1}{2}$, where ii selects the component of the $\mathbf{A_2}$ ($i = 0$ for x, $i = 1$ for y etc.). This parameter has equal properties to the orientation order parameter S_2.

Experimental setup

In the measurement setup, a high-precision motorized syringe pump drove the flow of the CNC suspension through a glass capillary at a selected volumetric flow rate. (Images of the experimental setup are presented in the supplementary material.) The inner diameter of the capillary was 1.6 mm and the length 100 mm. From the capillary, the flow discharged into a small container from where it was pulled back into the syringe for the next discharge flow. OCT scanned the flow in the capillary over a 2D cross-section perpendicular to the capillary axis at a position close to the end of the capillary. The 2D scan was done as a series of one-dimensional scans shown as red lines in the schematic drawing of Fig. 2. For each 1D scan, the OCT device deflected the light ray with movable and turnable galvanic mirrors. The lens used in the OCT device was of a telecentric type, thus all the light rays left the device in the same direction. In this study, one 2D scan consisted of 250 1D scans spanning 3.0 mm. The frequency of 1D scans was 5.5 kHz.

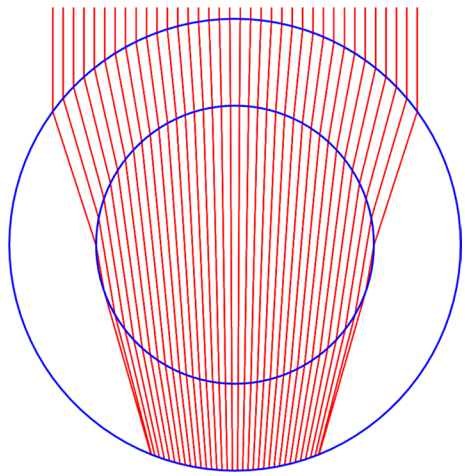

Fig. 2 The path of light rays traveling in the capillary and the CNC suspension

While traveling in the capillary system, each light ray was refracted at phase interfaces due to changes in the optical index of refraction, which changed the speed of light as well. In the 2D images recorded by the OCT device, each column corresponds to a single 1D scan while each row corresponds to time-of-light coordinate along the light rays (red lines of Fig. 2). The index of refraction for the capillary glass and for the CNC suspension were chosen so that the shape of the inner capillary wall in the computed image and in the scanned image best matched (see Fig. 4). Values used in this study were 1.5 for glass and 1.35 for CNC

suspension. Due to the complex path of light rays, the shape of the circular capillary was deformed in the OCT images. In particular, in the OCT images the flow channel seems to be close to 2 mm wide.

Results and discussion

We begin this section by reporting and discussing the experimental PS-OCT retardation data for different flow rates. Then we will move on to show comparisons of the data against the power-law model. Next, we will report the power-law model parameters, and discuss their values and implications on the connection between the shear rate and the particle orientation. Finally, we present the results given by the orientation model.

Retardation images from PS-OCT

The data measured for the CNC suspensions at different concentrations and flow rates are reported in Fig. 3. The data shows clear asymmetry in the vertical direction (the direction of the OCT beam). A few tests were run where the beam was rotated by 45 degrees from the vertical direction, or the whole measurement setup was rotated 45 degrees around the capillary axis. In all these tests, the scanned images remained unchanged. Thus we can be conclude that neither gravity nor flow field asymmetry is causing the observed asymmetry in the retardation data. Comparing the images row-wise shows that increasing the flow rate increases the retardation. Specifically, at the lowest concentration, no retardation is observed indicating that the particles are randomly oriented in the flow. Increasing the flow rate, the plots begin to show some modest phase shift, which is an indication of variation in the refractive index. In the present system, this variation may only be due to the particles orienting along the direction of the flow. Therefore, the PS-OCT data indicates a rational result: increasing the flow rate leads to better particle alignment.

The retardation in the images grows when the particle concentration in the suspension increases, i.e. comparing the images in Fig. 3 column-wise. This may occur due to a couple of reasons. First of all, at increased concentrations, the particles are forced to flow in the same orientation for extended periods of time due to the inter-particle interactions. Secondly, since there are more particles in the suspension, the difference in the refractive index is larger for the two polarizations even if the orientation distributions at different concentrations might be the same. However, from a random orientation distribution no retardation should be observed indicating that for the higher

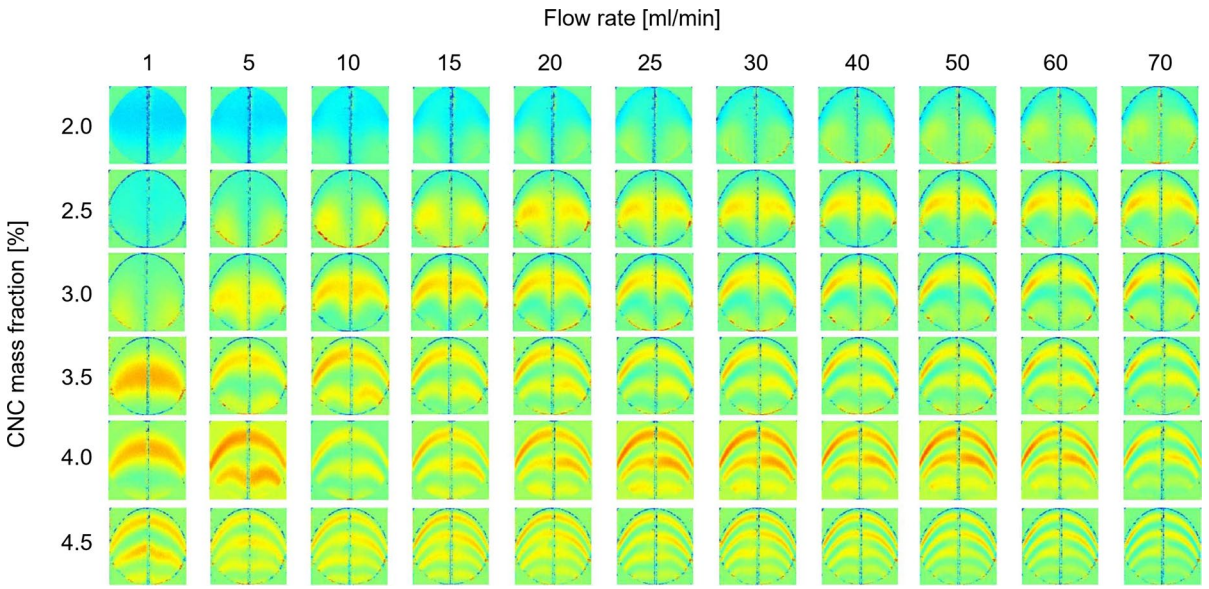

Fig. 3 The measured retardation at different flow rates and CNC mass fractions

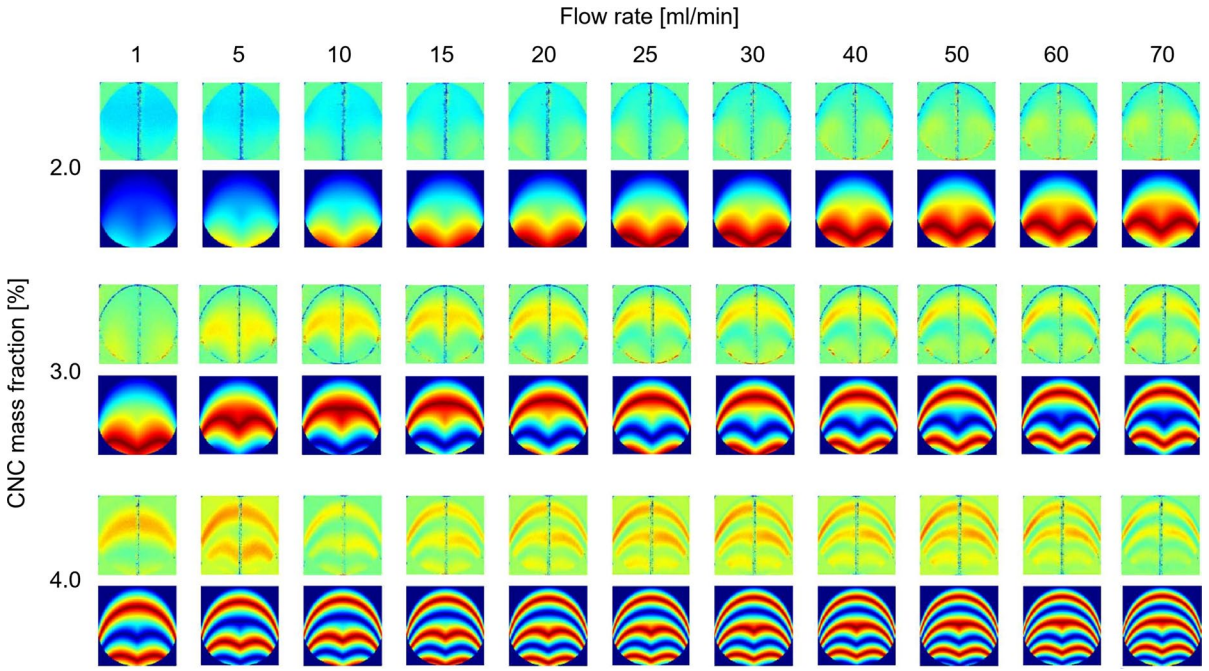

Fig. 4 The measured and simulated retardation at different mass fractions and flow rates

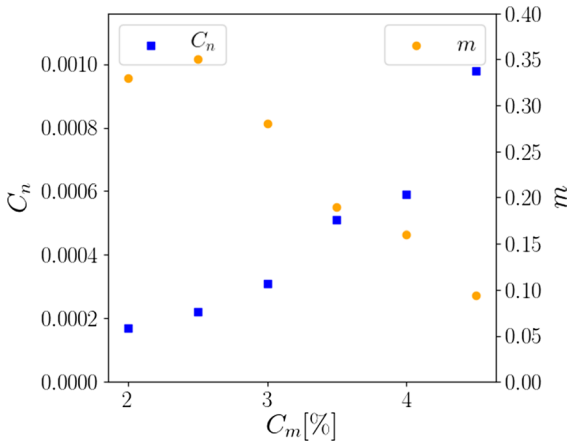

Fig. 5 The fitted optical model parameters as a function of the CNC concentration

concentrations already at the smallest flow rates certain degrees of alignment occurs.

Comparison against the power-law model

We computed retardation images from the power-law model Eq. 5 using the exponents and the pre-factors of fitting parameters. We compare the resulting images against their experimental counterparts in Fig. 4. For each concentration, fixed values of the parameters are applied for all flow rates. The modeled images correspond to their experimental counterparts remarkably well given the simplicity of the power-law model.

Next we turn our attention toward the fitted optical parameters. In Fig. 5 the parameters C_n and m are plotted as a function of the CNC concentration. The pre-factor C_n, which presumably takes into account the particle concentration, increases monotonically with the concentration and may be fitted by a quadratic function. The exponent m, describing the Δn sensitivity towards shear, decreases linearly between the concentrations 2.5 and 4.5 % w/w. This trend is feasible considering the orientation of particles in a sheared suspension. Before the CNC particles form liquid crystal phases, the interaction between the particles tends to increase the orientation disorder (the orientation diffusion parameter in orientation models (Folgar and Tucker III 1984)), which nicely corresponds to the behavior of m observed here.

With a fixed orientation distribution of nanocrystals, the absolute birefringence Δn scales linearly

with the amount of crystals. Thus, it is convenient to study normalized birefringence $\Delta n/\Phi$ where Φ is the volume fraction of crystals. The normalized birefringence can be expressed in the form $\Delta n/\Phi = \delta n_0 \times S_2$, where δn_0 is the specific birefringence of the crystals suspended in water and S_2 is the orientation order parameter described in "Orientation model" section.

We calculated the normalized birefringence from Eq. (5) with parameter values presented in Fig. 5. Here we used shear rate 1000 1/s, which is a characteristic maximum value at the capillary wall realized in our experiments. The volume fraction Φ was calculated by scaling the mass fraction with the crystallite density 1.5 g/cm^3. Calculated values of the normalized birefringence varied from 0.06 to 0.15, which are of the same order as the specific birefringence $\delta n_0 = 0.12$ reported by Frka-Petesic et al. (2015) for fully aligned tunicin cellulose nanocrystals. Thus we can expect considerable amount of orientation in our study, even though we cannot calculate the exact value of the order parameter due to unknown value of the specific birefringence for the CNC grade used in this study.

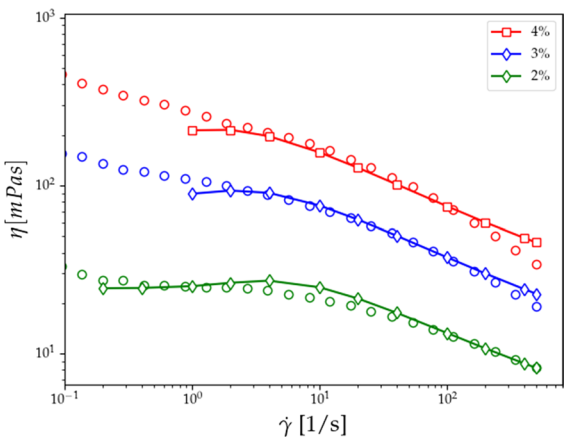

Fig. 6 The modeled and experimental flow curves for different CNC concentrations. As the plots show, the lowest concentration is rather well described by the orientation model, while for the larger concentrations the model performance is rather poor. The model parameters are $N_p = 1550$, $D_r = 0.08$, $N_p = 714$, $D_r = 0.12$, and $N_p = 231$, $D_r = 0.19$, for 4%, 3%, and 2% mass fractions, respectively

Orientation model

Next, we turn our attention to the orientation model and the way it reflects the experimental findings and the power-law model. First, we fit a scalar version of the orientation model against the measured flow curves of the nanocrystal suspensions. This assumes a homogeneous simple shear flow field within the rheometer geometry, characterised by a scalar global average shear rate. We realize that at this point we make the assumption that the velocity profile in the rheometer is homogeneous, which might not be accurate given the tendency of non-Newtonian flows to display shear banding and wall slip. In cellulose based suspensions this typically occurs specifically at small shear rates. The fits simulated using the orientation model against the measured curves are plotted in Fig. 6. Specifically at high shear rates, which correspond to the range where the capillary experiments are performed, the model deviates somewhat from the experiments–this may be related to the aggregation of CNC particles, a feature absent in the present model (Ma et al. 2008).

The change in the refractive index is proportional to the flow directional component of the $\mathbf{A_2}$ orientation tensor. This may be used to compute the retardation images applying the orientation model data in the ray tracing already implemented for the power-law model. The retardation images thus obtained are plotted in Fig. 7. These should be compared against the ones plotted in the top row of Fig. 4. This comparison shows that the retardation based on the orientation model is far less sensitive to the flow rate than that in the power-law model and the experiment. This deficiency might relate to either the mentioned absence of the aggregation effects, or shear-induced particle

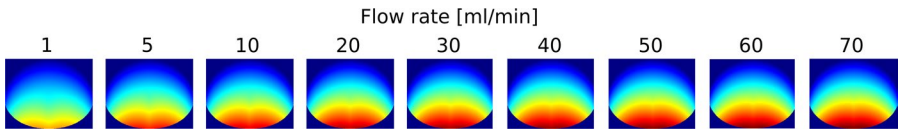

Fig. 7 The retardation images simulated using the orientation model. Here, the concentration is 2.0 % and the flow rates are 1, 5, 10, 20, 30, 40, 50, 60, and 70 mL/min

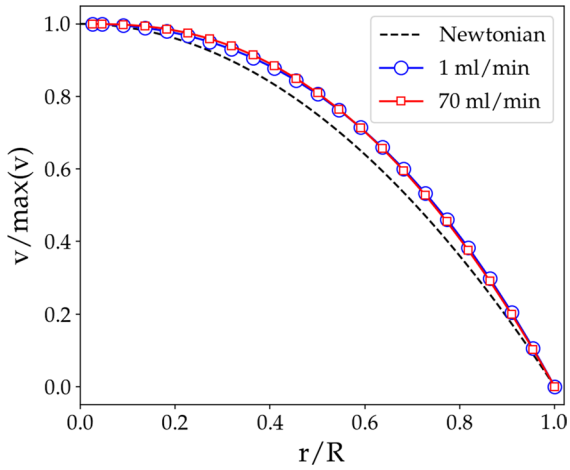

Fig. 8 Velocity profiles for the smallest and largest flow rates of 1 and 70 mL/min. The profiles are close to the Newtonian velocity profile and show no signs of shear banding

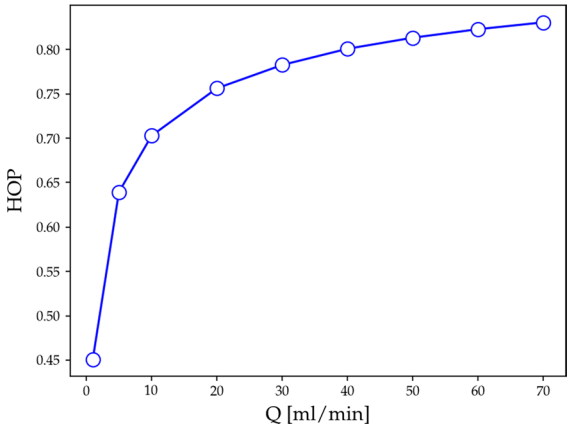

Fig. 9 Hermans' orientation parameter as a function of the flow rate as computed from the orientation model. Largest changes in the orientation parameter occur at relatively low flow rates

diffusion, a known property of particle suspensions, where concentration gradients appear due to differences in the local shear rate (Phillips et al. 1992; Korhonen et al. 2015). Such concentration gradients are not possible to implement in the present formulation of the model, which does not explicitly consider particle concentration in the equations, but rather hides the effect of these in the parameters N_p and D_r.

The simulated velocity profiles scaled by the maximum velocity at the center and the tube radius are plotted in Fig. 8. Such a scaling reveals that the profiles are close to the Newtonian parabolic one. This occurs due to the fact that the flow rates are relatively large making the viscosity of the 2 % suspension rather low and therefore the differences in the local viscosity small. Only minor flattening of the profile compared to the Newtonian one may be observed while almost no differences in the shapes between the different flow rates can be observed.

Now the question of how the tube flow influences the overall orientation of the particles remains. Computing the Hermans' orientation parameter and weighting that based on the mass fraction of the flowing suspension allows for computing the "mean" orientation of the particles over the whole capillary. These are plotted in Fig. 9. This shows that initially, the orientation parameter increases quickly with increasing flow rate, but plateaus rather early on, as was observed also in the computed retardation images. This suggests that indeed the retardation images and the overall orientation are descriptors of the same property.

Conclusions

In this article we have discussed polarization-sensitive optical coherence tomography (PS-OCT) as a light-weight online measurement tool, which can be used to observe the orientation of elongated particles, such as cellulose nanocrystals, during processing. An advantage of OCT is the possibility to get local information, which is useful when developing non-trivial flow geometries e.g. for 3D printing and flow focusing.

Being able to assess the orientation on the fly is the first step that will enable the development of adjustable flow geometries that allow faster adaptation of new fiber based material combinations and recipes to such manufacturing techniques. We envision for instance a universal 3D printing device allowing a wide range of different fiber materials to be incorporated on fly.

In addition, we have shown how to interpret the retardation images obtained from the measurement and how they may be connected to the particle alignment during flow. This interpretation is further reinforced by our simulations, which show that indeed the flow rheology may be described relatively well by an

orientation model. In addition, such a model could be used to compute the retardation images in qualitative agreement with the experimental data.

There are several interesting options for future work. For 3D printing of CNC-reinforced structures, it is often important to maximize the CNC orientation in the nozzle and minimize their disorientation in the outflow (Gauss et al. 2021). In the future PS-OCT could give new possibilities for optimizing the outflow conditions to maximize the orientation. Cellulose nanofibrils (CNFs) are a potential raw material for strong filaments (Lundahl et al. 2017). One open question here is why a very long capillary may be needed to maximize the strength of the filaments (Mohammadi et al. 2017). As the oriented structures of CNFs exhibit birefringence (Rosén et al. 2020; Lasseuguette et al. 2008), PS-OCT could be used for the analysis of the development of CNF orientation during processing.

Author contributions All authors contributed to the study conception and design. Material preparation, data collection and analysis were performed by AJ and IL. The orientation model simulations were performed by AP. The first draft of the manuscript was written by AP and AK and all authors commented on previous versions of the manuscript. All authors read and approved the final manuscript.

Funding Open Access funding provided by Technical Research Centre of Finland (VTT). This work is part of the Academy of Finland's Flagship Programme under Project numbers 318890 and 318891 (Competence Center for Materials Bioeconomy, FinnCERES), and grant number 278367.

Declarations

Conflict of interest The authors have no relevant financial or non-financial interests to disclose.

References

Adachi Y, Di C, Xiao F, Kobayashi M (2019) Size, orientation, and strength of NA-montmorillonite flocs flowing in a laminar shear flow. Colloid Polym Sci 297(7):979–987

Advani SG, Tucker CL III (1987) The use of tensors to describe and predict fiber orientation in short fiber composites. J Rheol 31(8):751–784

Alizadehgiashi M, Khabibullin A, Li Y, Prince E, Abolhasani M, Kumacheva E (2018) Shear-induced alignment of anisotropic nanoparticles in a single-droplet oscillatory microfluidic platform. Langmuir 34:322–330

Blaser S (2000) Flocs in shear and strain flows. J Colloid Interface Sci 225(2):273–284

Butler JE, Snook B (2018) Microstructural dynamics and rheology of suspensions of rigid fibers. Annu Rev Fluid Mech 50:299–318

Chen Z, Milner TE, Dave D, Nelson JS (1997) Optical doppler tomographic imaging of fluid flow velocity in highly scattering media. Opt Lett 22(1):64–66

Chen S, Schueneman G, Pipes RB, Youngblood J, Moon RJ (2014) Effects of crystal orientation on cellulose nanocrystals-cellulose acetate nanocomposite fibers prepared by dry spinning. Biomacromol 15:3827–3835

de Boer JF, Milner TE (2002) Review of polarization sensitive optical coherence tomography and Stokes vector determination. J Biomed Opt 7(3):359–371

de Boer JF, Hitzenberger CK, Yasuno Y (2017) Polarization sensitive optical coherence tomography–a review [invited]. Biomed Opt Express 8(3):1838–1873

Dinh SM, Armstrong RC (1984) A rheological equation of state for semiconcentrated fiber suspensions. J Rheol 28(3):207–227

Drexler W, Fujimoto JG (2008) Optical coherence tomography–technology and applications

Folgar F, Tucker CL III (1984) Orientation behavior of fibers in concentrated suspensions. J Reinf Plast Compos 3(2):98–119

Frka-Petesic B, Sugiyama J, Kimura S, Chanzy H, Maret G (2015) Negative diamagnetic anisotropy and birefringence of cellulose nanocrystals. Macromolecules 48(24):8844–8857

Fuller GG (1990) Optical rheometry. Annu Rev Fluid Mech 22:387–417

Gauss C, Pickering KL, Muthe LP (2021) The use of cellulose in bio-derived formulations for 3D/4D printing: a review. Compos Part C Open Access 4:100113–100128

George J, Sabapathi S (2015) Cellulose nanocrystals: synthesis, functional properties, and applications. Nanotechnol Sci Appl 8:45–54

Gowda K, Brouzet C, Lefranc T, Söderberg LD, Lundell F (2019) Effective interfacial tension in flow-focusing of colloidal dispersions: 3D numerical simulations and experiments. J Fluid Mech 876:1052–1076

Gunes D, Scirocco R, Mewis J, Vermant J (2008) Flow-induced orientation of non-spherical particles: effect of aspect ratio and medium rheology. Non-Newtonian Fluid Mech 155:39–50

Habibi Y, Lucia LA, Rojas OJ (2010) Cellulose nanocrystals: Chemistry, self-assembly, and applications. Chem Rev 110(6):3479–3500

Hausmann M, Rühs P, Siqueira G, Läuger J, Libanori R, Zimmermann T, Studart A (2018) Dynamics of cellulose nanocrystal alignment during 3D printing. ACS Nano 12(7):6926–6937

Hee MR, Huang D, Swanson EA, Fujimoto JG (1992) Polarization-sensitive low-coherence reflectometer for birefringence characterization and ranging. J Opt Soc Am B 9(6):903–908

Hindmarsh AC, Brown PN, Grant KE, Lee SL, Serban R, Shumaker DE, Woodward CS (2005) SUNDIALS: suite of nonlinear and differential/algebraic equation solvers. ACM Trans Math Softw (TOMS) 31(3):363–396

Ingber M, Mondy L (1994) A numerical study of three-dimensional Jeffery orbits in shear flow. J Rheol 38(6):1829–1843

Kádár R, Spirk A, Nypelö T (2021) Cellulose nanocrystal liquid crystal phases: progress and challenges in characterization using rheology coupled to optics, scattering, and spectroscopy. ACS Nano 15(5):7931–7945

Kim K, Patrick Kim RA, Chowdhury Jand, Kantharaj R, Candadai A, Marconnet A, Pol V, Youngblooda J (2021) Structural orientation effect of cellulose nanocrystals (CNC) films on electrochemical kinetics and stability in lithium-ion batteries. Chem Eng J 417:128128

Koponen A, Haavisto S (2020) Analysis of industry-related flows by optical coherence tomography–a review. Kona Powder Part J 37:42–63

Korhonen M, Mohtaschemi M, Puisto A, Illa X, Alava MJ (2015) Apparent wall slip in non-Brownian hard-sphere suspensions. Eur Phys J E 38(5):1–9

Lasseuguette E, Roux D, Nishiyama Y (2008) Rheological properties of microfibrillar suspension of tempo-oxidized pulp. Cellulose 15:425–433

Leahy BD, Koch DL, Cohen I (2017) Controlling the alignment of rodlike colloidal particles with time-dependent shear flows. J Rheol 61(5):979–996

Lundahl MJ, Klar V, Wang L, Mariko Ago M, Rojas OJ (2017) Aligning cellulose nanofibril dispersions for tougher fibers. Ind Eng Chem Res 56(1):8–19

Ma W, Chinesta F, Ammar A, Mackley M (2008) Rheological modeling of carbon nanotube aggregate suspensions. J Rheol 52(6):1311–1330

Mason S, Manley RSJ (1956) Particle motions in sheared suspensions: orientations and interactions of rigid rods. Proc R Soc Lond A 238(1212):117–131

Mohammadi P, Toivonen M, Ikkala O, Wagermaierm W, Linder BM (2017) Aligning cellulose nanofibril dispersions for tougher fibers. Sci Rep 7:11860–11869

Parker R, Guidetti G, Williams C, Zhao T, Narkevicius A, Vignolini S, Frka-Petesic B (2018) The self-assembly of cellulose nanocrystals: hierarchical design of visual appearance. Adv Mater 30:1704477

Petrie CJ (1999) The rheology of fibre suspensions. J Nonnewton Fluid Mech 87(2–3):369–402

Phillips RJ, Armstrong RC, Brown RA, Graham AL, Abbott JR (1992) A constitutive equation for concentrated suspensions that accounts for shear-induced particle migration. Phys Fluids A 4(1):30–40

Pignon F, Magnin A, Piau JM, Fuller G (2003) The orientation dynamics of rigid rod suspensions under extensional flow. J Rheol 47(2):371–388

Pujari S, Rahatekar S, Gilman J, Koziol K, Windle A, Burghardt W (2011) Shear-induced anisotropy of concentrated multiwalled carbon nanotube suspensions using x-ray scattering. J Rheol 55:1033–1058

Reising A, Moon R, Youngblood J (2012) Effect of particle alignment on mechanical properties of neat cellulose nanocrystal films. J Sci Technol For Prod Process 2(6):32–41

Rosén T, Brouzet C, Roth SV, Lundell F, Söderberg LD (2018) Three-dimensional orientation of nanofibrils in axially symmetric systems using small-angle x-ray scattering. J Phys Chem C 122(12):6889–6899

Rosén T, Wang R, Zhan C, He H, Chodankar S, Hsiao BS (2020) Cellulose nanofibrils and nanocrystals in confined flow: single-particle dynamics to collective alignment revealed through scanning small-angle x-ray scattering and numerical simulations. Phys Rev E 101(3):032610–032616

Sawada D, Nishiyama Y, Röder T, Porcar L, Zahra H, Trogen M, Sixta H, Hummel M (2021) Process-dependent nanostructures of regenerated cellulose fibres revealed by small angle neutron scattering. Polymer 218(18):123510

Sepehr M, Carreau PJ, Moan M, Ausias G (2004) Rheological properties of short fiber model suspensions. J Rheol 48(5):1023–1048

Shafiei-Sabet S, Hamad WY, Hatzikiriakos SG (2012) Rheology of nanocrystalline cellulose aqueous suspensions. Langmuir 28(49):17124–17133

Shrestha S, Montes F, Schueneman GT, Snyder JF, Youngblood JP (2018) Effects of aspect ratio and crystal orientation of cellulose nanocrystals on properties of poly(vinyl alcohol) composite fibers. Compos Sci Technol 167:482–488

Swanson E, Lin C, Schuman J, Stinson W, Chang W, Hee M, Flotte T, Gregory K, Puliafito C, Fujimoto J (1991) Optical coherence tomography. Science 254:1178–1181

Tatsumi M, Teramoto Y, Nishio Y (2015) Different orientation patterns of cellulose nanocrystal films prepared from aqueous suspensions by shearing under evaporation. Cellulose 22:2983–2992

Tsvetkov NV, Lebedeva EV, Lezov AA, Perevyazko I, Petrov MP, Mikhailova ME, Lezova AA, Torlopov MA, Krivoshapkin V (2017) Hydrodynamic and optical characteristics of hydrosols of cellulose nanocrystals. Colloid Polym Sci 295:13–24

Wiesauer K, Pircher M, Götzinger E, Hitzenberger CK, Engelke R, Ahrens G, Grützner G, Stifter D (2006) Transversal ultrahigh-resolution polarization-sensitive optical coherence tomography for strain mapping in materials. Opt Express 14(13):5945–5953